HHS Public Access

Author manuscript

Adv Mater. Author manuscript; available in PMC 2020 March 01.

Published in final edited form as:

Adv Mater. 2019 March ; 31(10): e1806899. doi:10.1002/adma.201806899.

3D Bioprinted In Vitro Metastatic Models via Reconstruction of Tumor Microenvironments

Fanben Meng,
Department of Mechanical Engineering, University of Minnesota, Minneapolis, MN 55455, USA

Carolyn. M. Meyer,
Division of Blood and Marrow Transplantation, Department of Pediatrics, University of Minnesota, Minneapolis, MN 55455, USA

Daeha Joung,
Department of Mechanical Engineering, University of Minnesota, Minneapolis, MN 55455, USA

Daniel. A. Vallera,
Department of Radiation Oncology, University of Minnesota, Minneapolis, MN 55455, USA

Michael. C. McAlpine,
Department of Mechanical Engineering, University of Minnesota, Minneapolis, MN 55455, USA

Angela Panoskaltsis-Mortari
Division of Blood and Marrow Transplantation, Department of Pediatrics, University of Minnesota, Minneapolis, MN 55455, USA

Abstract

The development of 3D in vitro models capable of recapitulating native tumor microenvironments could improve the translatability of potential anticancer drugs and treatments. Here, 3D bioprinting techniques are used to build tumor constructs via precise placement of living cells, functional biomaterials, and programmable release capsules. This enables the spatiotemporal control of signaling molecular gradients, thereby dynamically modulating cellular behaviors at a local level. Vascularized tumor models are created to mimic key steps of cancer dissemination (invasion, intravasation and angiogenesis), based on guided migration of tumor cells and endothelial cells in the context of stromal cells and growth factors. The utility of the metastatic models for drug screening is demonstrated by evaluating the anticancer efficacy of immunotoxins. These 3D vascularized tumor tissues provide a proof-of-concept platform to i) fundamentally explore the molecular mechanisms of tumor progression and metastasis, and ii) preclinically identify therapeutic agents and screen anticancer drugs.

mcalpine@umn.edu.

Experimental Section
The detailed experimental process is available in the Supporting Information.

Supporting Information
Supporting Information is available from the Wiley Online Library or from the author.

Conflict of Interest
The authors declare no conflict of interest.

Graphical Abstract

A migration-inducing, vascularized tumor model platform is created via 3D bioprinting of cells, natural hydrogels, and programmable release capsules. These cell-laden architectures are designed to recapitulate the primary characteristics of metastasis. The 3D models both physically and chemically reconstruct the tumor microenvironments with high spatiotemporal resolution, offering a tool to bridge the gap between monolayer cell culture and animal models.

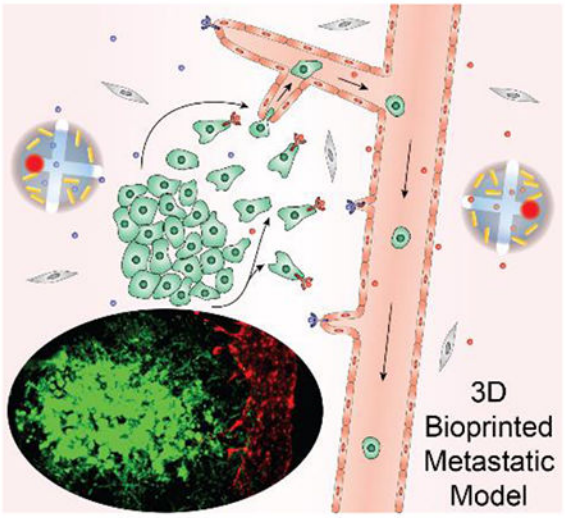

Keywords

3D printing; bioprinting; cell migration; drug screening; metastatic cancer model; tumor microenvironment; Tumor Models

A major challenge in the clinical translation of potential anti-cancer drugs and treatments is the discrepancy in the in vitro to in vivo efficacy of candidates.[1] Indeed, models using conventional 2D cell culture monolayers on flat surfaces often have difficulty in accurately recapitulating the characteristics of native tumor microenvironments.[2,3] To better capture the specificity and complexity of living tissues, 3D culture platforms have been developed to re-establish physiological cell–cell and cell–extracellular matrix (ECM) interactions.[2–7] Recent studies have demonstrated that 3D cultured tumor cells, typically cell spheroids and hydrogel scaffolds, more closely mimic their natural behaviors in vivo at both phenotypic and genotypic levels, and in their response to anticancer drugs.[5–10] However, other components, including stromal cells,[11] endothelial cells,[12] and immune cells,[13] also significantly contribute to tumor development and progression. 3D coculture of tumor cells and fibroblasts has further improved the overall biological relevance of in vitro models.[14–16] The introduction of microfluidic systems as vascularized models has provided valuable insights into tumor invasion, intravasation and extravasation.[17–20] Many challenges still remain in reconstructing microenvironments, where tumors originate, with precise spatial placement and arrangement of numerous critical components. More critically, the metastatic nature of cancer remains a major prognostic and therapeutic challenge[21] and these physical translocations of tumor cells are regulated by various chemical signals.[22]

Engineering a migration-inducing chemical microenvironment is indispensable for the creation of a feasible in vitro platform to address metastatic studies,[3,22] which has not yet been achieved by current tumor models. Hence, there is a need to develop more precise models that incorporate these elements of tumor microenvironments for the study of multilevel interactions that occur at adjacent and distant sites.[23]

3D bioprinting provides a novel approach to the design and fabrication of complex tissue constructs in vitro.[24–28] It allows for the integration of numerous combinations of living cells and supporting matrices with precise spatial control, resulting in the engineering of numerous tissues with promising biomedical applications.[29–37] The bioprinting technique has been demonstrated to offer new possibilities in advancing cancer research by creating vascularized tissues[26,33,38,39] and positioning tumor cell-laden hydrogels.[40,41] 3D printing has also been used to construct dynamic chemical environments: biomolecular gradients can be created and manipulated within matrices via the programmable release of 3D printed stimuli-responsive core/shell capsules.[42] These capsules are comprised of an aqueous core with a payload of functional molecular factors and a biocompatible polymer shell containing plasmonic gold nanorods (AuNRs). The aqueous cores maintain the activities of the biomolecular payloads, while the photothermal response of the AuNRs permits selective rupturing of the capsules when irradiated with a resonant laser wavelength determined by the aspect ratio of the nanorods. This approach allows for both spatial (via the 3D printing) and temporal (via the triggered release) generation of chemical cues in 3D matrices, enabling postprint dynamic regulation of cellular behaviors at a local level. Combining these 3D printing approaches with 3D cellular bioprinting may provide a promising combination of tools to create complex tumor constructs accompanied by multiplexed chemical signals, with high spatiotemporal resolution,[43] beyond what is possible with conventional fabrication technologies.

In this study, our objective was to design and construct in vitro tumor models via physical and chemical means to approximate the tumor microenvironment properties critical to several key components of metastatic dissemination, including invasion, intravasation and angiogenesis. By taking advantage of 3D bioprinting, clusters of tumor cells, stromal cells, and infused vascular cells were precisely placed according to their physiological functions. Meanwhile, extracellular chemical gradients were dynamically manipulated via 3D printed, nanomaterial-functionalized, stimuli-responsive capsules containing growth factors, enabling postprint cellular modulation. As a proof of concept, we demonstrate that these vascularized constructs can serve as versatile preclinical tools for high-throughput anticancer drug screening.

The conceptual design of the metastatic models is illustrated in Scheme 1. First, extracellular biomolecular gradients are dynamically generated within 3D hydrogel matrices via controllable release of 3D printed stimuli-responsive microcapsules, mimicking chemical environments in tumor tissues and directing cell migration. Second, perfusable vessels are introduced to provide vascular conduits, allowing for the study of tumor cell intravasation through an endothelial barrier, thus resulting in circulating tumor cells (CTCs). Finally, multiple chemotactic pathways are programmed to guide both tumor cell invasion and angiogenesis, creating a metastatic model to recapitulate the initiation of cancer spreading.

The concept of modularity was utilized to construct these models. Individual bioprinted modules with specific physiological functions were assembled to reconstruct tumor microenvironments (Scheme 1), which included i) the tumor cell droplet as the primary tumor, ii) the endothelialized microchannel as the vascular conduit, iii) the fibroblast-laden natural hydrogel as the tumor stroma, and iv) 3D printed programmable release capsules as the sources of chemical signal gradients.

3D printed programmable release capsules triggered by laser irradiation (Figure 1a),[42] developed in our previous work, were used to both temporally and spatially create gradients of chemotactic agents. In order to simulate the dynamic chemical environment of tumor tissue, the stimuli-responsive core/shell capsules were designed to meet the following criteria: i) the biomolecular release and gradient maintenance should match the timescale of cellular activities; ii) the stimulation that triggers payload release should not affect the viability of cells; and iii) activities of biomolecular payloads should be retained both before and after laser-triggered release.

To match the timescale of potential cellular activities in this study, rather than using a viscous aqueous solution, the crosslinked gelatin methacrylate (GelMA) hydrogel was chosen as the supporting material for cores, owing to its previously demonstrated application in controlled drug release.[34,44] Meanwhile, poly(lactic-*co*-glycolic) acid (PLGA) shells were functionalized by AuNRs as photothermal agents with absorption at 700 nm, in order to respond to a near-infrared (NIR) laser of wavelength 783 nm. This mismatch of wavelength is attributed to the redshift of the localized surface plasmon resonance (LSPR) peak, ranging from ≈50 to100 nm, when AuNRs are incorporated into a polymer film with a refractive index greater than aqueous solutions.[42] The utilization of a NIR laser and the localized heating arising from absorption in the AuNRs are expected to minimize any side effects of irradiation on cell viability and activity of biomolecular payloads.[42,45] Natural fibrin hydrogel was chosen as the 3D matrix, serving as a main component of the stroma in the tumor models due to its biocompatibility and biodegradability, allowing cells to remodel their own extracellular microenvironments.[46]

Epidermal growth factor (EGF), a well-known chemoattractant of carcinoma cells involved in tumor progression,[47] was encapsulated to test the feasibility of spatiotemporal control of payload release from the core/shell capsules. The laser-triggered progression of gradual EGF (Texas red-labeled) release from a single capsule over a 2-day period within the fibrin gel is shown in Figure 1b and quantitated by the time-dependent decrease of fluorescence intensity within the capsule (Figure 1c, red curve). As expected, the capsules preserved growth factor payload within the polymer shell before laser rupture (black curve). Compared to payload release from bare cores (blue curve), a low level of passive leakage was detected from capsules, which may be due to slow hydrolysis of PLGA within the hydrogel matrix. To demonstrate spatial control with the capsules, we printed arrays of cores containing varying volumes. Figure 1d shows a representative linear array of EGF capsules with 750 μm center-to-center spacing covered by a fibrin gel. The volumes of the printed capsules were controlled with nanoliter resolution via tuning the dispensing time. Capsules were sequentially ruptured using a NIR laser. Fluorescence (Figure 1d) and brightfield (Figure

S1a, Supporting Information) images show that individual capsules could be precisely triggered, demonstrating high-resolution spatial control over payload release.

Next, we investigated whether released growth factors could form and retain a chemical gradient within a 3D fibrin gel. Due to the impracticality of noninvasively performing an accurate assessment of molecular concentration within a hydrogel matrix, we instead designed two built-in chambers (I and II) located at each end of the fibrin gel, allowing us to independently measure the levels of EGF that collected in the culture medium contained in the chambers. The relative locations of chambers are depicted in the inset of Figure 1e, and the design of the entire test chamber is shown in Figure S1b (Supporting Information). As shown in Figure 1e, the level of EGF detected in Chamber I (closer to the capsule) was always higher than in Chamber II (further away), after laser-rupturing the printed capsule. A significant difference could be observed 6 h following release of EGF and was maintained until at least 48 h (Figure S1c, Supporting Information), which indicated the generation of an EGF gradient within the fibrin gel. Both progressive molecule release at a moderate rate and relatively slow diffusion within the gel may contribute to the retention of this gradient. Thus, by combining the advantages of both temporal and spatial manipulation of molecular gradients, these 3D bioprinted programmable release capsules provide an approach to chemically reconstruct dynamic extracellular microenvironments in 3D hydrogel matrices.

We next determined whether the EGF gradients generated by programmable release capsules could be used to guide tumor cell migration, the most critical step in metastasis.[48] As shown in Figure 2a, a droplet of fibrin loaded with green fluorescent protein (GFP)-A549 lung cancer cells (carcinoma) was printed between linear arrays of chemoattractant capsules (right) and blank control capsules (left), within a designed culture chamber (Figure 2b). The linear array was aligned to induce one-way cell migration. The 3D printed chamber allowed us to test five groups of migration samples in parallel under identical conditions. In a typical configuration, the printed droplet defined the primary site of the tumor cells. To generate a long-lasting EGF gradient, capsules were ruptured sequentially at 2-day intervals, starting with the capsule closest to the cell droplet. Concomitantly, a corresponding control capsule was also ruptured. It should be mentioned that PLGA shells undergo slow hydrolysis within the hydrogel, causing limited passive release of payloads. The capsule array design (Figure 2a) using increasing volumes overcomes this potential influence on the gradient formation.

Panoramic fluorescence images (Figure 2c, Movie S1, Figure S2a in the Supporting Information showing mono field of view images) show the distributions of A549s over a 10-day period after rupturing the first pair of EGF and control capsules. By comparing the cell distributions at each time point (Figure 2c), there are three observations to describe the cellular activities: i) increased proliferation; ii) expansion in space; and iii) directional movement. Most of the escaped cells were only found in the EGF capsule region and increased in number as more EGF capsules were ruptured, demonstrating guided cell migration. A parallel control experiment without laser rupture revealed that most of the A549s remained within the original site without any directional migratory behavior (Figure S2b, Supporting Information).

The cellular growth rates were quantitatively compared between samples with and without laser-triggered release of EGF by directly analyzing the fluorescence intensity of GFP-expressing cells. As shown in Figure 2d, the growth of tumor cells was accelerated in response to released EGF, consistent with previous reports.[49] The migratory behavior was further quantified by tracking the positions of individual A549 cells or clusters (Figure S2c and Movie S2, Supporting Information). To show that the migration was guided and directional, the horizontal travel distance of leading cells over time was calculated (Figure 2e). Under the guidance of EGF cues, the maximum cell velocity was $15.48 \pm 1.05\ \mu m\ h^{-1}$, in contrast with control capsules which exhibited random movement of cells with a maximum velocity of $1.21 \pm 0.57\ \mu m\ h^{-1}$ (approximately one order of magnitude slower). These results strongly suggest that EGF released from the 3D printed capsules not only actively promoted the proliferation of A549 cells, but also guided their migration.

To demonstrate the versatility and selectivity of this platform, in parallel we monitored the activities of GFP-expressing M4A4 cells (a melanoma cell line), as well as red fluorescent protein (RFP)-expressing human umbilical vein endothelial cells (HUVECs, a vascular endothelial cell line), in response to EGF capsules sequentially ruptured over 10 days (Figure S2d,e, Supporting Information). Figure 2f shows that although M4A4s could travel further due to their more aggressive nature, these cells also exhibited directional movement, supporting the versatility of our model. Specificity was confirmed by the negative migratory response of HUVECs to EGF gradients. These results confirm that the migration of tumor cells was effectively guided by using 3D printed programmable release capsules as dynamic chemoattractant sources.

Together with the dynamic chemical environment, the vascular path, a common route of metastasis, is another key component of a biomimetic tumor model, as illustrated in Scheme 1. A microchannel created using the pin-molding technique with the support of a designed culture chamber (Figure 3a) was endothelialized by direct injection of HUVEC suspensions via capillary action (Figure 3b), and the patency of the vessel lumen was demonstrated by perfusion of a fluorescent dye-labeled fluid (tuned to a viscosity similar to blood by adding glycerol) and the absence of instantaneous leakage into the surrounding matrix (Figure 3c).

To mimic the metastatic cascade in the context of cell types relevant to the tumor microenvironment, we functionalized the vascularized 3D matrix to include spatiotemporal control over both tumor cell invasion and angiogenesis as illustrated in Scheme 1. By taking advantage of 3D printing in terms of spatial control, a droplet of A549-laden fibrin, simulating primary tumor, was placed 1 mm away from the vessel between microcapsule arrays, while fibroblasts were integrated into the surrounding hydrogel as supporting stromal cells, promoting the remodeling of extracellular matrix. Figure 3d presents a typical bioprinted tumor model. The viability of A459s and HUVECs after printing and injection, respectively, was analyzed (postfabricated viability > 93%; Figure S3, Supporting Information), suggesting that the fabrication processes minimally impact cells within bioprinted models.

In addition to tumor cell-attracting EGF, vascular endothelial growth factor (VEGF), a well-known angiogenic mediator,[47] was also introduced to promote and direct the formation of a

vascular network from a pre-existing uniaxial vessel, as illustrated in Scheme 1. The images in Figure 3e (Figure S4a–d in the Supporting Information shows mono field of view images) show the sprouting process from an existing vessel. Via laser-triggered release of VEGF, numerous endothelial cells sprouted from the vessel. The sprouts extended with longer culture time and as more VEGF capsules were ruptured, and the formed vasculature could be maintained for ≈2 weeks. These daughter vessels were only observed on the side of the mother vessel where VEGF capsules were printed, consistent with the angiogenic process being guided by VEGF gradients generated from the capsules. To further confirm this conclusion, we directly mixed VEGF in the gel without the formation of molecular gradients, and sprouts were found to randomly distribute on either side of the mother vessel (Figure S4e, Supporting Information).

Since it is possible that the tumor cells and endothelial cells may cross-signal to each other through cell-secreted mediators, we first verified the source of the growth factors. We confirmed by quantitative polymerase chain reaction (qPCR) that HUVECs within fibrin gels did not express EGF when cultured alone or in coculture with A549s (Figure 3f). Tumor cells are known to secrete proangiogenic factors, such as VEGF, to activate endothelial cells of pre-existing blood vessels.[50] When cultured alone, A549s expressed VEGF, but the expression was not enhanced with the introduction of HUVECs. The protein concentrations of the growth factors secreted from the cells were also measured, and the results were consistent with gene expression analysis. EGF protein concentration was below the limit of detection in all samples, whereas 12.8 ± 0.3 and 5.1 ± 2.4 pg mL^{-1} VEGF were detected in 3D monocultured A549s and 3D cocultured A549s/HUVECs, respectively. The measured levels of VEGF were significantly lower than previously reported concentrations that were shown to induce endothelial sprouts in vitro,[51] and also at least two orders of magnitude lower than the level of growth factor released from a single printed capsule. These results all suggest that the capsules are necessary to maintain the chemical gradient for the in vitro models. Furthermore, the introduction of both growth factors (VEGF and EGF) to cocultured samples caused the increase of VEGF receptor (VEGFR) expression in HUVECs, and EGF receptor (EGFR) expression in A549s (comparing red and blue bars in Figure 3f), indicating the active responses of the cells to the applied factors. Similar results were seen when M4A4s were used in place of A549s, confirming that the results are not specific to the cancer cell line (Figure S5, Supporting Information).

To initiate metastatic dissemination in the model, EGF capsules were sequentially ruptured to guide tumor cell invasion and migration, while VEGF was released to modulate sprouting angiogenesis, via NIR laser irradiation with high spatial control (see the Supporting Note in the Supporting Information for a discussion on the safety concerns of laser irradiation). Figure 3g shows the cellular migration patterns in response to these growth factors over time and demonstrates that both tumor cell invasion and angiogenesis were directed toward one another. With time, more A549s migrated into the fibroblast-laden fibrin between the tumor cell droplet and the formed vasculature, while a few tumor cells were found in the main vessel, indicating their intravasation (days 9 and 12) and spread. It should be noted that these guided behaviors of tumor and endothelial cells were also seen when fibroblasts were not incorporated within the surrounding fibrin gel (Figure S6, Supporting Information), further confirming the critical function of released growth factors in the process. Although there is

no direct evidence to clarify whether fibroblasts mediated tumor cell intravasation in this study, these stromal cells did contribute to maintaining the hydrogel matrix, as fibrin gel could be gradually degraded by tumor cells, especially in the M4A4 model.

Interestingly, the tumor cells that intravasated into the main vascular conduit started to travel with fluidic flow as CTCs and could be collected within an independent chamber (Figure 3h). This metastatic cell collection chamber was designed to access one end of the main vessel, which was separated from the main chamber of the structured cell-laden gel by an impermeable silicone wall (relative chamber positions in Figure 3a and Figure S7 in the Supporting Information). Since these two chambers could only communicate through the endothelialized microchannel, the observation of A549s within the collection chamber further confirmed the intravasation of tumor cells originating from the primary bioprinted tumor droplet. Figure 3h shows that the number of disseminated tumor cells positively correlated to tissue culture time. This is likely due to both the metastasis and subsequent proliferation of disseminated cells, identifying an enriched population of metastatic cells that can be analyzed for specific CTC characteristics. To verify that the collected A549 cells were consistent with metastatic cells, the expression of vimentin and N-cadherin–known markers of carcinoma progression–was analyzed by qPCR.[52,53] To demonstrate this progression, as shown in the bar chart of Figure 3h (inset), both vimentin and N-cadherin of A549s in bioprinted tumor droplets were upregulated in response to EGF released from capsules (comparing blue bars to gray bars), indicating the potential of EGF-responsive cells for increased malignancy.[54] The expression of the two metastatic markers in disseminated A549s within the collection chambers was significantly increased further (red bars) compared to the EGF-exposed cells remaining in the gel, confirming that the EGF-induced relocation of tumor cells resembled metastatic dissemination and enrichment of CTCs. Thus, this model dynamically mimics the processes of invasion and intravasation, suggesting a promising tool to explore potential targets for future therapies.

We further tested the feasibility of our in vitro metastatic 3D models as preclinical testbeds. Since the tumor models are vascularized, in vivo drug delivery can be mimicked by introducing drugs through the built-in vessel. We tested two immunotoxins that were developed in previous studies,[55–57] to demonstrate the screening ability for targeted therapy. The two drugs were designed to share the same toxin fragments but target different cell types. The first ligand-directed toxin, EGF4KDEL, consists of EGF and truncated *Pseudomonas* exotoxin with a C-terminus of Lys-Asp-Glu-Leu (KDEL) cloned as a single-chain molecule and targets EGFR-overexpressing A549s. Following the introduction of EGF4KDEL through the main vessel, the growth of tumor cells was significantly reduced compared to no drug treatment, and neither guided invasion nor migration was observed (Figure 4a). The former demonstrates the potency of the engineered drug, while the latter exhibits the competition between the EGF-linked toxin and the EGF released from printed capsules, both suggesting that the tumor progression was impeded, consistent with the previous in vivo animal studies.[55,56] Another ligand-directed toxin, CD22KDEL, was used as an off-target control. In CD22KDEL, the targeting domain is an anti-CD22 single-chain variable fragment that binds to the transmembrane protein CD22 specific to B cells. Since A549s do not express CD22, they were not affected by CD22KDEL, similar to the no treatment control, showing fast proliferation and guided invasion as expected (Figure 4a).

Growth curves shown in Figure 4b were generated by quantitatively analyzing the fluorescence intensity of A549s, while tumor cell invasions were quantified by tracking the leading cells (Figure S8a, Supporting Information). The potency and targeting of anticancer drugs could be compared over time, as shown in Figure 4c and Figure S8b (Supporting Information). These results all support the feasibility of using 3D bioprinted tumor models as preclinical tools for drug screening.

To highlight the advantage of the 3D tumor models in simulating in vivo microenvironments for target cells, we compared the anticancer effects of the immunotoxin in the 3D bioprinted tumor model (Figure 4a) to 2D monolayer cultured A549s (Figure S9a, Supporting Information). The plots in Figure 4d show relative tumor cell viability with the introduction of EGF4KDEL. Intriguingly, the death rate of tumor cells in the 3D models was lower, compared to 2D cultured cells on a flat plastic substrate. This observation is consistent with previous reports on the effect of dimensionality.[9,10] However, our model introduces an endothelial barrier as well as stromal cells. As shown in Figure 4d and Figures S9b,c (Supporting Information), tumor cells in the presence of fibroblasts exhibited lower proliferation and lower sensitivity to targeting toxins. This implies a slower diffusion rate and/or potential binding of drugs by fibroblasts when incorporated in the gel (acting as a sink). Therefore, these 3D tumor models could provide more meaningful insights into the in vivo cellular response to drugs–including cell-cell and cell-ECM interactions, endothelial permeability of drugs, and the influence of stroma–compared to conventional 2D monolayer culture.

In this study, we have demonstrated the utility of a 3D tumor model platform created by bioprinting methods, with the incorporation of a functional vasculature and stromal elements. Guided cell migration and angiogenesis through programmed release capsules provide a system to dynamically study metastatic processes, while functional vasculature enables the introduction of tumor-targeting agents, rendering the platform amenable to drug-screening applications. The incorporation of collection chambers into the design allows for the study of CTCs that “self-select” in the metastatic process.

Compared to conventional 2D monolayer culture, our 3D bioprinted metastatic tumor models retain the advantages of other 3D cell culture systems while adding other unique features. First, the introduction of fibroblasts can facilitate matrix remodeling.[11] Second, the built-in vessel offers a tool to study transendothelial behaviors of tumor cells and allows for the introduction of drug candidates through an endothelial barrier, mimicking in vivo drug delivery.[58] Third, the model design enables the collection of CTCs that self-select to intravasate. Finally, cell-cell interactions can be actively guided via biochemical cues generated at a local level. When compared to other reported vascularized tumor models, [17–20] the model presented here exhibits several notable advantages. The first is the development of vasculatures from the guided sprouting angiogenesis of a main vessel with a diameter of several hundred micrometers to enable a multiscale network, ranging from venules to capillaries. Second, in terms of parenchyma, tumor cells were printed as cell cluster droplets, which can spatially define primary sites and yield more insights into dynamic processes of tumor progression. Third, different from microfabrication-based techniques, 3D (bio)printing avoids harsh chemicals and thus is more amenable to materials

and geometry, in order to construct complex tumor tissues with irregular structures. Finally, the integration of programmable release capsules imbues the capability of postfabricated modification of 3D printed tumor models via the chemotaxis of cells. This effectively adds a fourth dimension (temporal control) to 3D tumor models. Even though these printed tumor models are simplified and cannot fully recapitulate the complexity of the in vivo tumor microenvironment, they show the potential to provide valuable insights into clinical translatability beyond traditional laboratory animals[1–4,59] in the following aspects: i) the in vitro models are totally comprised of human cells; ii) simplified chemical environments, especially the capsule system, allow for the reduction to a few isolated chemical factors, making it more convenient to define molecular mechanisms, iii) the vasculatures within these models are uniaxial with a length less than 1 cm, wherein drugs can rapidly target tumor cells; and iv) ethical issues are minimized by using in vitro models for toxicity assays.

It is well known that the tumor environment is a complex system with multilevel interactions between numerous components. In addition to tumor parenchymal cells, fibroblasts, and blood vessels, which have been incorporated within our current models, important constituents, such as innate and adaptive immune cells, lymphatic vessels, pericytes, and other stromal cells, also contribute to these microenvironments.[13] Although the simplicity of the current printed tumor model favorably identifies fundamental problems in the preclinical setting as mentioned above, rational, stepwise integration of more constituents will enable improvements in the optimization of the heterogeneity within a tumor-simulating model. The flexibility to add functional materials in our extrusion-based 3D printing process may provide possible solutions, as does the ability to precisely place different combinations of tumor-relevant cells and hydrogel matrices. Moreover, owing to this flexibility in materials and cells, these in vitro models can be customized with patient-specific designs and functionalities by directly using cells collected from individuals.

In summary, we report a new 3D bioprinting-mediated method for the creation of migration-inducing, vascularized tumor models, aiming to bridge the gap between 2D monolayer cell culture and animal models. These 3D cell-laden architectures were fabricated to capture the primary characteristics of the metastatic translocation of tumor cells in vitro. The preclinical application was demonstrated by the effective screening of targeting immunotoxins with anticancer efficacy. The 3D engineered models both physically and chemically reconstruct the microenvironments of tumors with high spatiotemporal resolution, which offer tools to i) advance 3D tissue engineering for dynamic mimicking of the in vivo natural microsystem with capabilities of postfabricated modulation, ii) further understand the mechanisms of metastatic dissemination, iii) screen novel anticancer drugs, and iv) test patient-specific strategies for diagnosis and therapeutics.

Supplementary Material

Refer to Web version on PubMed Central for supplementary material.

Acknowledgements

The authors thank Michael J. Ehrhardt for performing EGF and VEGF assays in the Cytokine Reference Laboratory (University of Minnesota, CLIA’88 licensed facility: #24D0931212), Daniel C. Sorby from the 3D Bioprinting

Facility (University of Minnesota) for providing printing consumables, and Dr. Jakub Tolar for providing fibroblasts. F.M. was partially supported by a Cancer Bioengineering Fellowship from the Physical Sciences in Oncology Center (PSOC) at the University of Minnesota. The study was supported by the National Institute of Biomedical Imaging and Bioengineering of the National Institutes of Health (Award No. 1R21EB022830) awarded to A.P.-M., a seed grant from the UMN Institute for Engineering in Medicine, and a Pilot Project award from the UMN Prostate and Urologic Cancer Translational Workgroup. M.C.M acknowledges the National Institute of Biomedical Imaging and Bioengineering of the National Institutes of Health (Award No. 1DP2EB020537). The content is solely the responsibility of the authors and does not necessarily represent the official views of the National Institutes of Health.

References

[1]. Vanderburgh J, Sterling JA, Guelcher SA, Ann. Biomed. Eng 2017, 45, 164. [PubMed: 27169894]

[2]. Pampaloni F, Reynaud EG, Stelzer EHK, Nat. Rev. Mol. Cell Biol 2007, 8, 839. [PubMed: 17684528]

[3]. Griffith LG, Swartz MA, Nat. Rev. Mol. Cell Biol 2006, 7, 211. [PubMed: 16496023]

[4]. Bian S, Repic M, Guo Z, Kavirayani A, Burkard T, Bagley JA, Krauditsch C, Knoblich JA, Nat. Methods 2018, 15, 631. [PubMed: 30038414]

[5]. Fischbach C, Chen R, Matsumoto T, Schmelzle T, Brugge JS, Polverini PJ, Mooney DJ, Nat. Methods 2007, 4, 855. [PubMed: 17767164]

[6]. Rijal G, Li W, Sci. Adv 2017, 3, e1700764. [PubMed: 28924608]

[7]. Tian X, Werner ME, Roche KC, Hanson AD, Foote HP, Yu SK, Warner SB, Copp JA, Lara H, Wauthier EL, Caster JM, Herring LE, Zhang L, Tepper JE, Hsu DS, Zhang T, Reid LM, Wang AZ, Nat. Biomed. Eng 2018, 2, 443.

[8]. Lee GY, Kenny PA, Lee EH, Bissell MJ, Nat. Methods 2007, 4, 359. [PubMed: 17396127]

[9]. Hakanson M, Textor M, Charnley M, Integr. Biol 2011, 3, 31.

[10]. Horning JL, Sahoo SK, Vijayaraghavalu S, Dimitrijevic S, Vasir JK, Jain TK, Panda AK, Labhasetwar V, Mol. Pharmaceutics 2008, 5, 849.

[11]. Kalluri R, Zeisberg M, Nat. Rev. Cancer 2006, 6, 392. [PubMed: 16572188]

[12]. Reymond N, d'Água BB, Ridley AJ, Nat. Rev. Cancer 2013, 13, 858. [PubMed: 24263189]

[13]. Joyce JA, Pollard JW, Nat. Rev. Cancer 2009, 9, 239. [PubMed: 19279573]

[14]. Liu T, Lin B, Qin J, Lab Chip 2010, 10, 1671. [PubMed: 20414488]

[15]. Jeong S-Y, Lee J-H, Shin Y, Chung S, Kuh H-J, PLoS One 2016, 11, e0159013. [PubMed: 27391808]

[16]. Jaganathan H, Gage J, Leonard F, Srinivasan S, Souza GR, Dave B, Godin B, Sci. Rep 2014, 4, 6468. [PubMed: 25270048]

[17]. Jeon JS, Bersini S, Gilardi M, Dubini G, Charest JL, Moretti M, Kamm RD, Proc. Natl. Acad. Sci. U.S.A 2015, 112, 214. [PubMed: 25524628]

[18]. Chen MB, Whisler JA, Fröse J, Yu C, Shin Y, Kamm RD, Nat. Protoc 2017, 12, 865. [PubMed: 28358393]

[19]. Zervantonakis IK, Hughes-Alford SK, Charest JL, Condeelis JS, Gertler FB, Kamm RD, Proc. Natl. Acad. Sci. U.S.A 2012, 109, 13515. [PubMed: 22869695]

[20]. Du Z, Mi S, Yi X, Xu Y, Sun W, Biofabrication 2018, 10, 034102. [PubMed: 29786602]

[21]. Chaffer CL, Weinberg RA, Science 2011, 331, 1559. [PubMed: 21436443]

[22]. Roussos ET, Condeelis JS, Patsialou A, Nat. Rev. Cancer 2011, 11, 573. [PubMed: 21779009]

[23]. Infanger DW, Lynch ME, Fischbach C, Annu. Rev. Biomed. Eng 2013, 15, 29. [PubMed: 23642249]

[24]. Murphy SV, Atala A, Nat. Biotechnol 2014, 32, 773. [PubMed: 25093879]

[25]. Mannoor MS, Jiang Z, James T, Kong YL, Malatesta KA, Soboyejo WO, Verma N, Gracias DH, McAlpine MC, Nano Lett. 2013, 13, 2634. [PubMed: 23635097]

[26]. Kolesky DB, Homan KA, Skylar-Scott MA, Lewis JA, Proc. Natl. Acad. Sci. U.S.A 2016, 113, 3179. [PubMed: 26951646]

[27]. Cui H, Nowicki M, Fisher JP, Zhang LG, Adv. Healthcare Mater 2017, 6, 1601118.

[28]. Liu W, Zhang YS, Heinrich MA, De Ferrari F, Jang HL, Bakht SM, Alvarez MM, Yang J, Li Y-C, Trujillo-de Santiago G, Miri AK, Zhu K, Khoshakhlagh P, Prakash G, Cheng H, Guan X, Zhong Z, Ju J, Zhu GH, Jin X, Shin SR, Dokmeci MR, Khademhosseini A, Adv. Mater 2017, 29, 1604630.

[29]. Villar G, Graham AD, Bayley H, Science 2013, 340, 48. [PubMed: 23559243]

[30]. Pati F, Jang J, Ha D-H, Won Kim S, Rhie J-W, Shim J-H, Kim D-H, Cho D-W, Nat. Commun 2014, 5, 3935. [PubMed: 24887553]

[31]. Kang H-W, Lee SJ, Ko IK, Kengla C, Yoo JJ, Atala A, Nat. Biotechnol 2016, 34, 312. [PubMed: 26878319]

[32]. Colosi C, Shin SR, Manoharan V, Massa S, Costantini M, Barbetta A, Dokmeci MR, Dentini M, Khademhosseini A, Adv. Mater 2016, 28, 677. [PubMed: 26606883]

[33]. Miller JS, Stevens KR, Yang MT, Baker BM, Nguyen D-HT, Cohen DM, Toro E, Chen AA, Galie PA, Yu X, Chaturvedi R, Bhatia SN, Chen CS, Nat. Mater 2012, 11, 768. [PubMed: 22751181]

[34]. Johnson BN, Lancaster KZ, Zhen G, He J, Gupta MK, Kong YL, Engel EA, Krick KD, Ju A, Meng F, Enquist LW, Jia X, McAlpine MC, Adv. Funct. Mater 2015, 25, 6205. [PubMed: 26924958]

[35]. McCracken JM, Badea A, Kandel ME, Gladman AS, Wetzel DJ, Popescu G, Lewis JA, Nuzzo RG, Adv. Healthcare Mater 2016, 5, 1025.

[36]. Miri AK, Nieto D, Iglesias L, Goodarzi Hosseinabadi H, Maharjan S, Ruiz-Esparza GU, Khoshakhlagh P, Manbachi A, Dokmeci MR, Chen S, Shin SR, Zhang YS, Khademhosseini A, Adv. Mater 2018, 30, 1800242.

[37]. Joung D, Truong V, Neitzke CC, Guo S-Z, Walsh PJ, Monat JR, Meng F, Park SH, Dutton JR, Parr AM, McAlpine MC, Adv. Funct. Mater 2018, 28, 1801850.

[38]. Kolesky DB, Truby RL, Gladman AS, Busbee TA, Homan KA, Lewis JA, Adv. Mater 2014, 26, 3124. [PubMed: 24550124]

[39]. Pi Q, Maharjan S, Yan X, Liu X, Singh B, Genderen AM, Robledo-Padilla F, Parra-Saldivar R, Hu N, Jia W, Xu C, Kang J, Hassan S, Cheng H, Hou X, Khademhosseini A, Zhang YS, Adv. Mater 2018, 30, 1706913.

[40]. Zhao Y, Yao R, Ouyang L, Ding H, Zhang T, Zhang K, Cheng S, Sun W, Biofabrication 2014, 6, 035001. [PubMed: 24722236]

[41]. Pang Y, Mao SS, Yao R, He JY, Zhou ZZ, Feng L, Zhang KT, Cheng SJ, Sun W, Biofabrication 2018, 10, 044102. [PubMed: 30129928]

[42]. Gupta MK, Meng F, Johnson BN, Kong YL, Tian L, Yeh Y-W, Masters N, Singamaneni S, McAlpine MC, Nano Lett. 2015, 15, 5321. [PubMed: 26042472]

[43]. Moroni L, Burdick JA, Highley C, Lee SJ, Morimoto Y, Takeuchi S, Yoo JJ, Nat. Rev. Mater 2018, 3, 21. [PubMed: 31223488]

[44]. Nichol JW, Koshy ST, Bae H, Hwang CM, Yamanlar S, Khademhosseini A, Biomaterials 2010, 31, 5536. [PubMed: 20417964]

[45]. Mura S, Nicolas J, Couvreur P, Nat. Mater 2013, 12, 991. [PubMed: 24150417]

[46]. Seliktar D, Science 2012, 336, 1124. [PubMed: 22654050]

[47]. Arwert EN, Hoste E, Watt FM, Nat. Rev. Cancer 2012, 12, 170. [PubMed: 22362215]

[48]. Condeelis J, Segall JE, Nat. Rev. Cancer 2003, 3, 921. [PubMed: 14737122]

[49]. Bost F, McKay R, Dean N, Mercola D, J. Biol. Chem 1997, 272, 33422. [PubMed: 9407138]

[50]. Cristofanilli M, Charnsangavej C, Hortobagyi GN, Nat. Rev. Drug Discovery 2002, 1, 415. [PubMed: 12119743]

[51]. Shamloo A, Xu H, Heilshorn S, Tissue Eng. Part A 2012, 18, 320. [PubMed: 21888475]

[52]. Larue L, Bellacosa A, Oncogene 2005, 24, 7443. [PubMed: 16288291]

[53]. Nieman MT, Prudoff RS, Johnson KR, Wheelock MJ, Cell Biol J. 1999, 147, 631.

[54]. Shintani Y, Okimura A, Sato K, Nakagiri T, Kadota Y, Inoue M, Sawabata N, Minami M, Ikeda N, Kawahara K, Matsumoto T, Matsuura N, Ohta M, Okumura M, Ann. Thorac. Surg 2011, 92, 1794. [PubMed: 22051275]

[55]. Stish BJ, Oh S, Chen H, Dudek AZ, Kratzke RA, Vallera DA, Br. J. Cancer 2009, 101, 1114. [PubMed: 19755995]

[56]. Oh S, Stish BJ, Sachdev D, Chen H, Dudek AZ, Vallera DA, Clin. Cancer Res 2009, 15, 6137. [PubMed: 19789305]

[57]. Vallera DA, Oh S, Chen H, Shu Y, Frankel AE, Mol. Cancer Ther 2010, 9, 1872. [PubMed: 20530709]

[58]. Seo BR, DelNero P, Fischbach C, Adv. Drug Deliv. Rev 2014, 69-70, 205. [PubMed: 24309015]

[59]. Hutchinson L, Kirk R, Nat. Rev. Clin. Oncol 2011, 8, 189. [PubMed: 21448176]

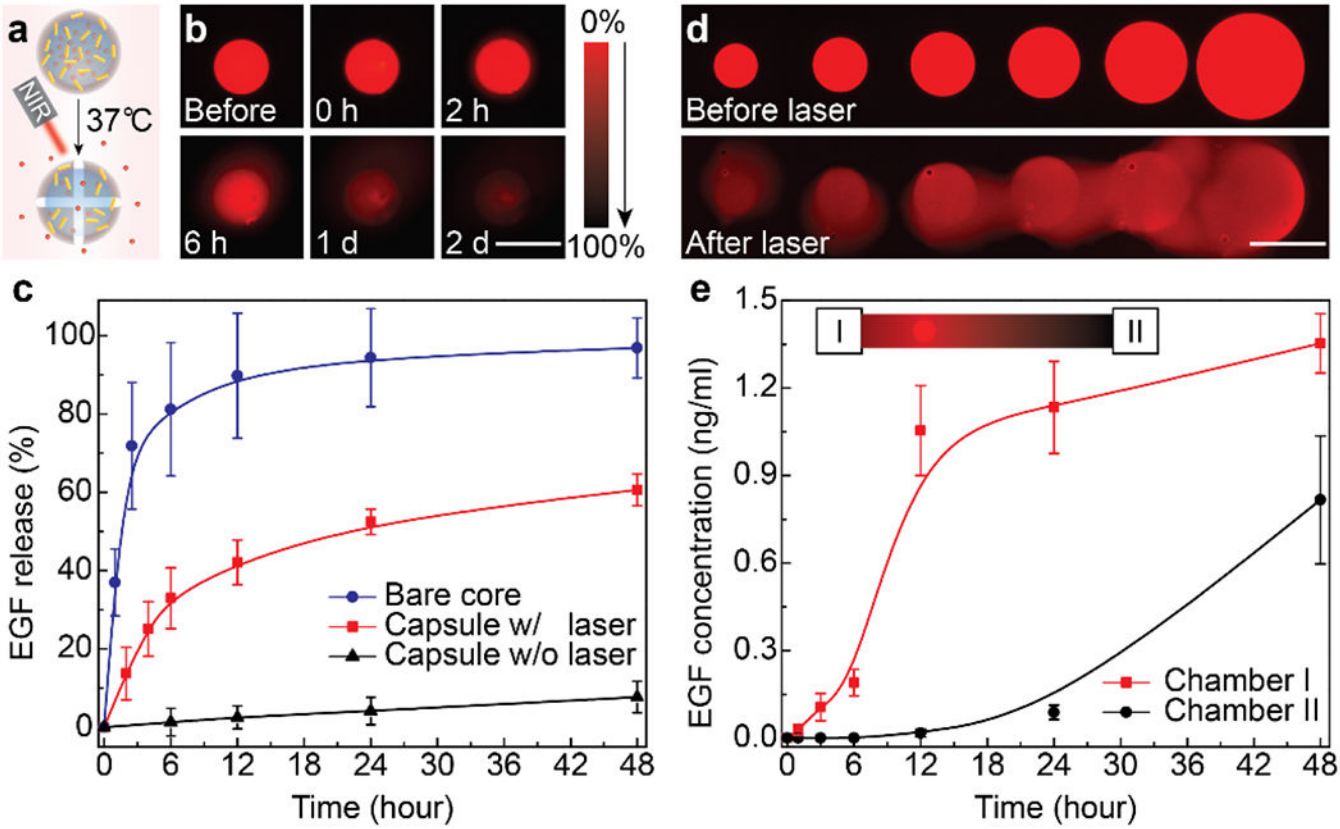

Figure 1.

Growth factor gradients generated by 3D printed programmable release capsules within a fibrin gel. a) Schematic images of laser-triggered release of growth factors from a printed core/shell capsule (core: growth factor-loaded GelMA hydrogel, shell: AuNR-functionalized PLGA film), when cultured at 37 °C. b) Time-lapse fluorescence images showing gradual release of Texas red-labeled EGF from a single capsule within the fibrin gel before and after laser irradiation. c) Plots showing release of EGF from a bare core (blue), a ruptured capsule (red) and a non-ruptured capsule (black), demonstrating the capability of temporal control over the payload release (100% was defined by the intensity of a blank capsule in the absence of Texas red-labeled EGF, mean ± standard deviation (s.d.), $n = 6$ per group). d) Panoramic fluorescence images of a linear array of Texas Red-EGF capsules with a center-to-center spacing of 750 μm and incremental size before (upper panel) and 6 h after (lower panel) laser irradiation. e) Plots of EGF concentration measured in Chamber I (3 mm to the EGF capsule, red) and II (9 mm to the EGF capsule, black) versus time, showing a gradient generated via laser-triggered release of an EGF capsule (mean ± s.d., $n = 4$ per group, inset: schematic images showing the relative positions between the capsule and chambers). Scale bar: 500 μm

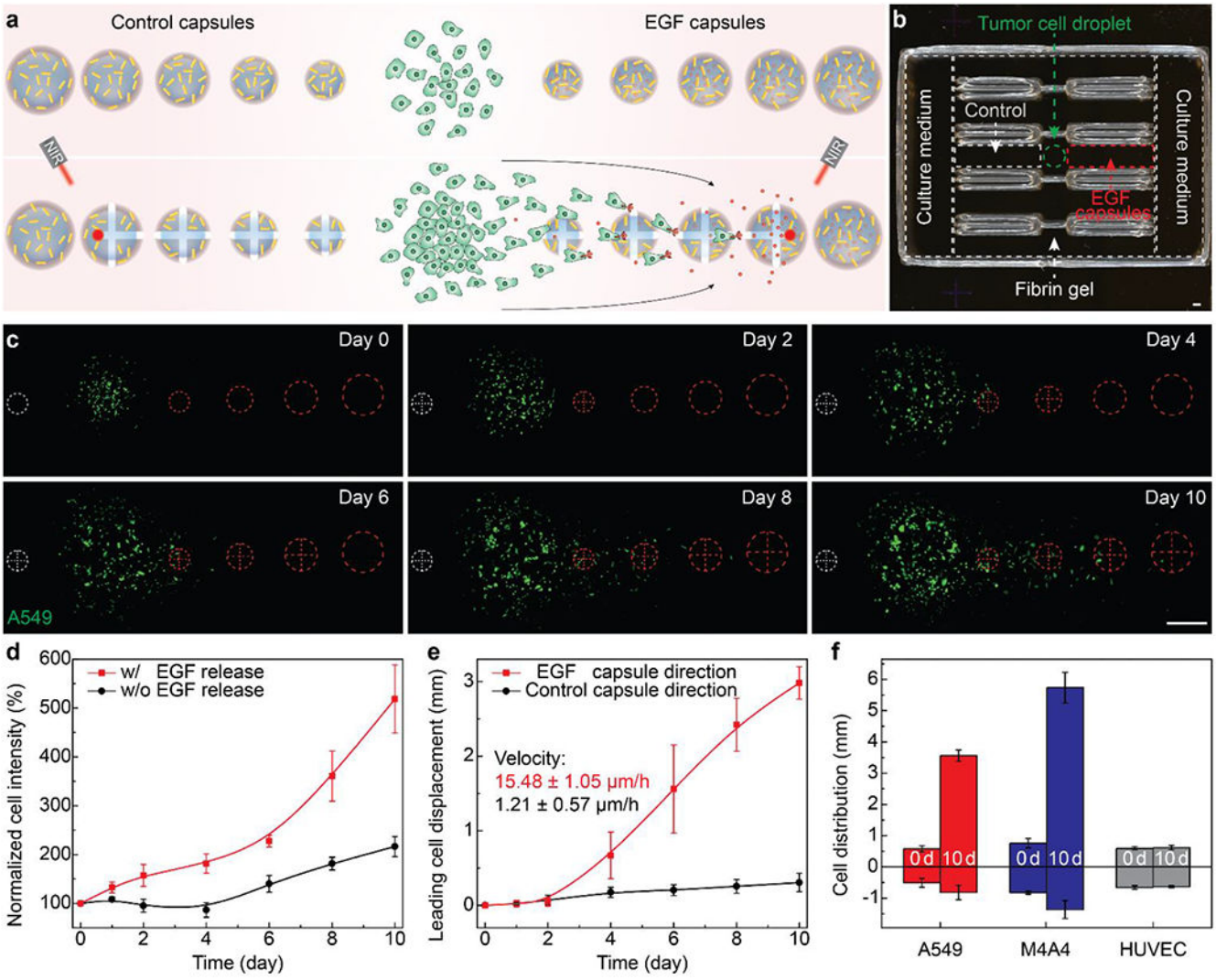

Figure 2.

Guided tumor cell migration with an EGF capsule array. a) Schematic image illustrating the directional migration of tumor cells under the guidance of EGF gradients generated by 3D printed capsules. b) Photo of a 3D printed culture chamber for tests of guided cell migration. c) Panoramic fluorescence images showing the distribution of GFP-expressing A549 cells over time, demonstrating the guided migration (red circles: EGF capsules; white circle: control capsule without growth factor loading; and cross lines: laser rupture pathways). d) Plots of cellular fluorescence intensity of A549s (normalized by intensity at day 0 before capsules were ruptured) versus time with (red) and without (black) EGF release, demonstrating the influence of EGF to cellular proliferation (mean ± s.d., $n = 4$ per group). e) Plots of the displacement of leading A549 cells (only the distance in the x-direction was measured) toward the EGF capsule direction (red) and control capsule direction (black) (mean ± s.d., $n = 4$ per group). f) Bar chart of distributions of GFP-A549s (red), GFP-M4A4s (blue), and RFP-HUVECs (gray) on day 10, showing the selective directed migration of tumor cells but not HUVECs (mean ± s.d., $n = 4$ per group). Scale bar: 500 μm

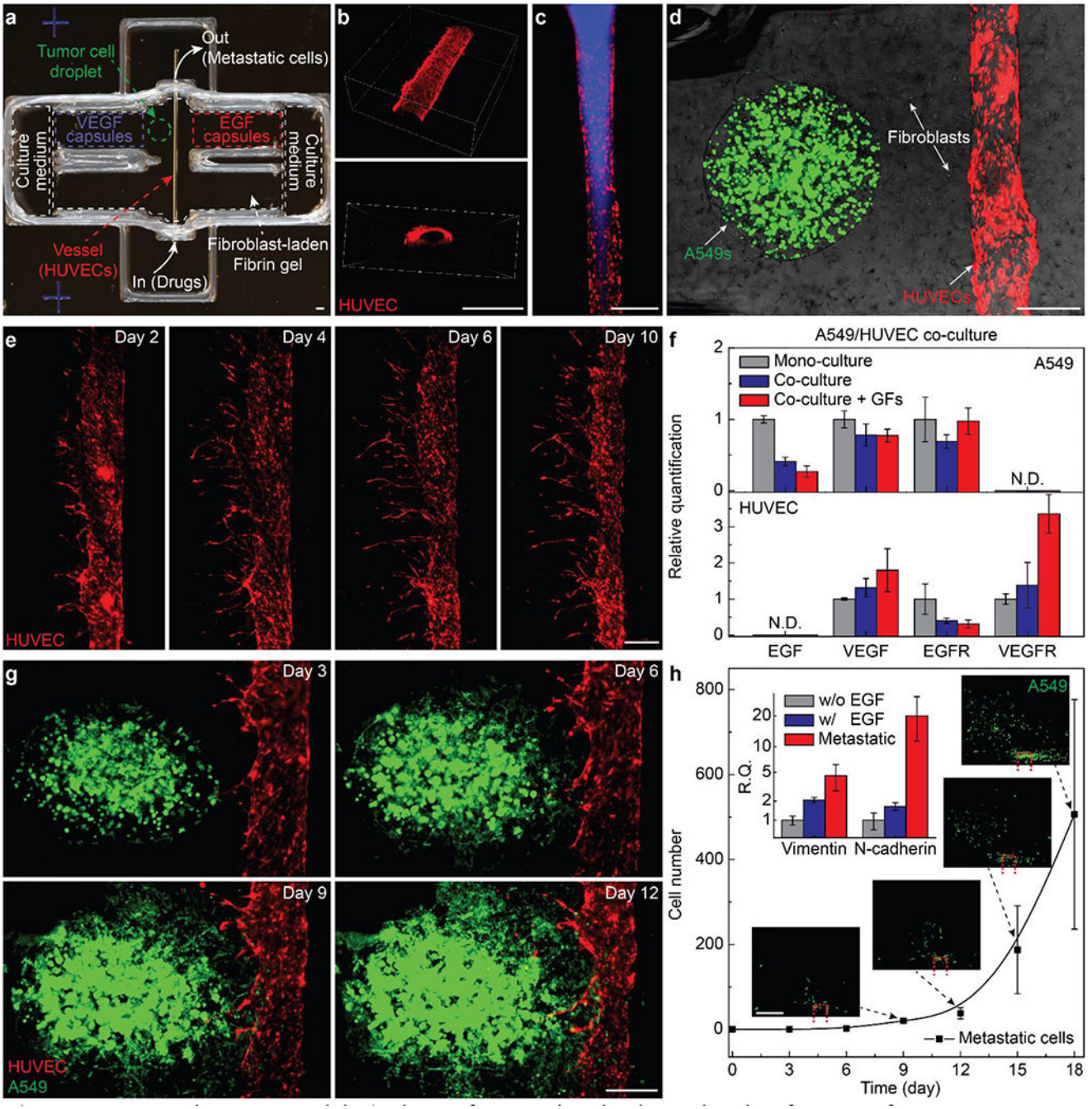

Figure 3.

Metastatic tumor model. a) Photo of a 3D printed culture chamber for tests of guided tumor cell dissemination. b) Confocal images of the top view (upper panel) and cross section (lower panel) of a representative microchannel lined by HUVECs within a fibrin gel, showing the lumen of the vessel. c) Fluorescence images showing a vessel perfused by fluorescent fluid (blue, recolored from poly(fluorescein isothiocyanate allylamine hydrochloride)). d) Composite image showing a representative tumor model before laser-triggered rupture of EGF and VEGF capsules (green fluorescence: GFP-expressing A549s,

red fluorescence: RFP-expressing HUVECs, bright field: fibroblasts). e) Panoramic fluorescence images showing sprouts generated from a main vessel and their extension toward a single direction over time, indicating guided sprouting angiogenesis by VEGF capsules. f) Bar chart showing the expression of EGF, VEGF, EGFR and VEGFR of A549s (upper panel) and HUVECs (lower panel) when mono cell-cultured (gray) and co-cell-cultured without (blue) and with (red) EGF and VEGF within fibrin gels (normalized by the levels of each mono cell-cultured samples, mean ± s.d., n = 3 per group, N.D.: nondetectable). g) Fluorescence images of a metastatic model on days 3, 6, 9 and 12, showing that A549s approach and enter the vasculature through the fibroblast-laden fibrin gel (green channel: GFP-expressing A549s, red channel: RFP-expressing HUVECs). h) Plots of the population of disseminated A549s detected in the collection chamber versus time. (mean ± s.d., n = 3 per group) Inset photos: fluorescence images showing the disseminated A549s in the collection chamber, with the red dash frame showing the vessel position. Inset bar chart: expression of vimentin and N-cadherin of 3D bioprinted A549s in tumor models without (gray) and with (blue) EGF release, and metastatic tumor cells (red) harvested in collection chambers (normalized by the levels of each untreated tumor model, mean ± s.d., n = 4-6 per group, R.Q.: relative quantification). Scale bar: 500 μm

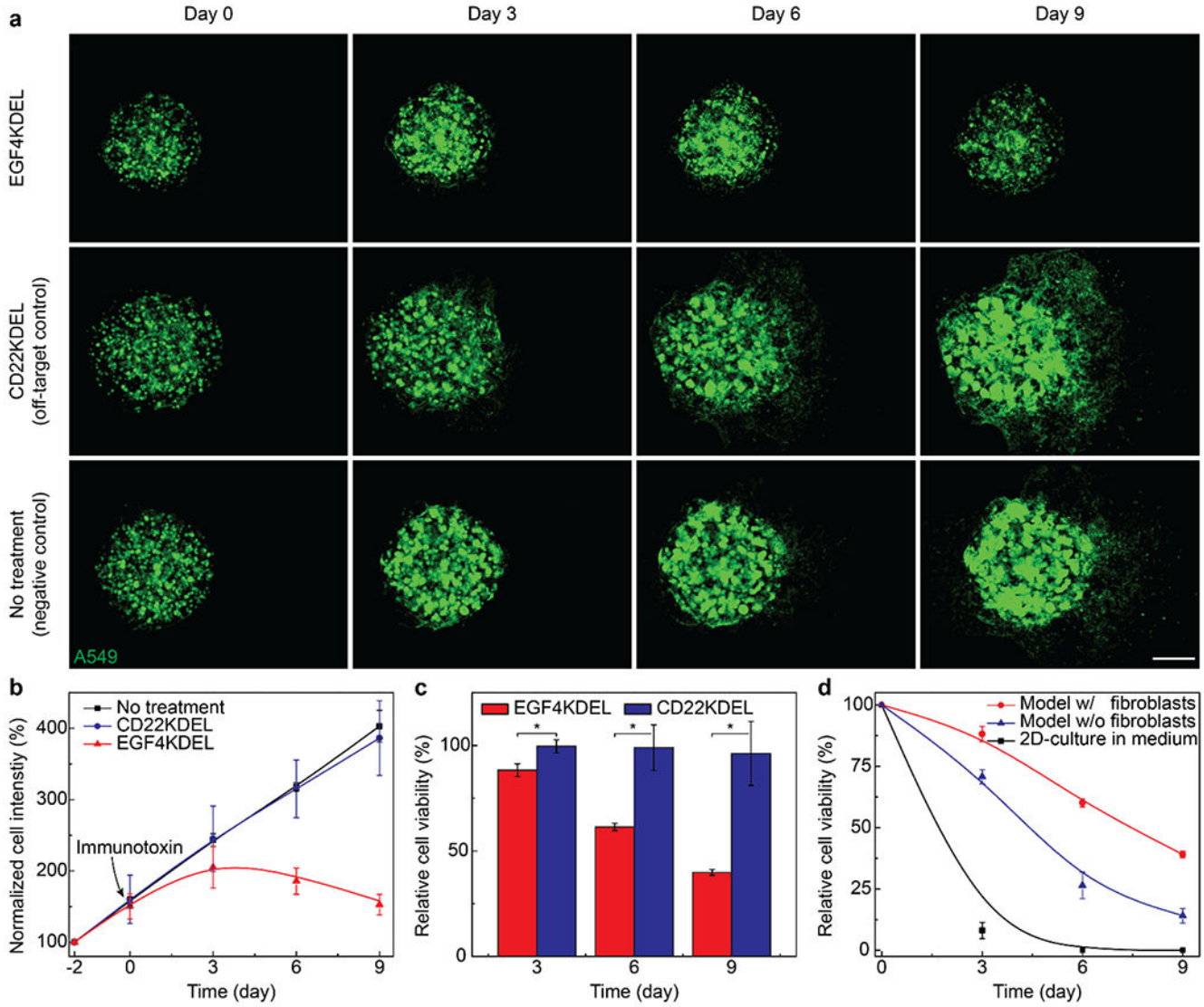

Figure 4.

Anti-cancer drug screening using the 3D metastatic models. a) Fluorescence images of printed A549s after immunotoxins were injected though a vessel within a fibroblast-laden fibrin gel, showing the effect of the drug over time. b) Plots of cellular fluorescence intensity of A549s (normalized by intensity at day 0 before immunotoxins were added) versus time without (black) and with treatment of toxins (red: target, blue: off-target), demonstrating the effect of drugs on cell viability (mean ± s.d., red: $n = 5$, blue and black: $n = 3$ on each day). c) Bar graph comparing the anticancer effect of immunotoxins over time, showing the drug screening application of the model (mean ± s.d., red: $n = 5$, blue: $n = 3$ on each day, $*p < 0.05$, day 3: $p = 0.002$, day 6: $p = 0.025$, day 9: $p = 0.023$, unpaired, two-tailed Student's t-test). d) Plots of relative cell viability (calculated by the ratio between the fluorescence intensity of treated models and parallel negative controls) of A549s versus time, showing the influence of the microenvironment on drug screening (mean ± s.d., red and black: $n = 5$, blue: $n = 3$ on each day). Scale bar: 500 μm

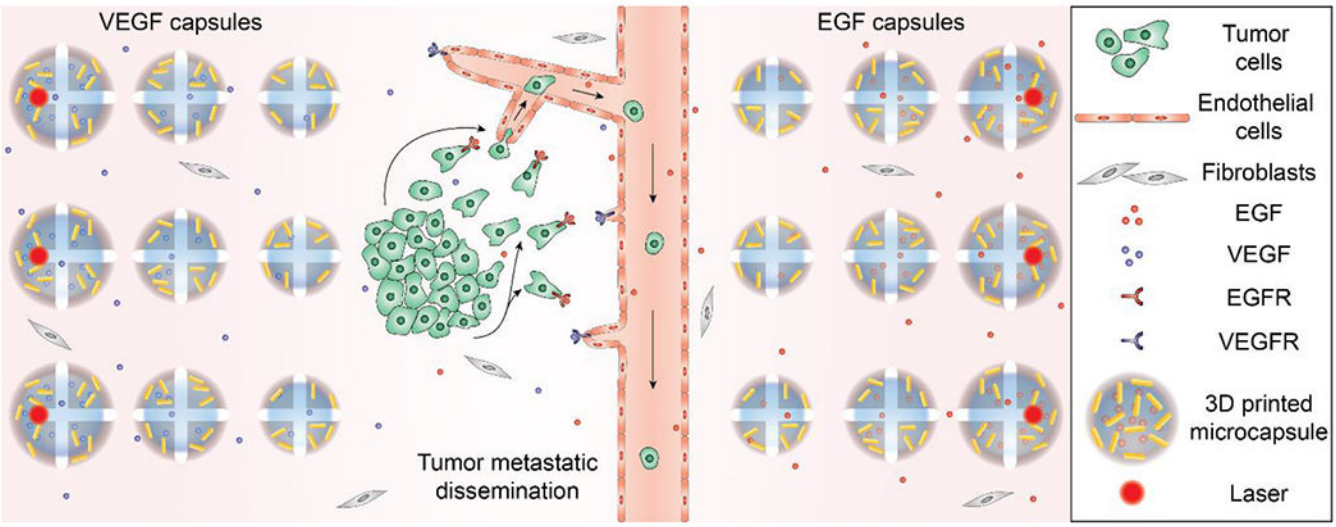

Scheme 1.

3D printed in vitro tumor models mimicking metastatic dissemination. Schematic image of the integration of tumor cells, endothelial cell-lined vascular conduits, and biochemical signals within a fibroblast-laden fibrin gel to reconstruct tumor microenvironments. Tumor cell invasion of the surrounding matrix and intravasation into the vasculature are mediated by EGF and VEGF gradients, which are dynamically generated by 3D printed programmable release capsules (EGF: epidermal growth factor; VEGF: vascular endothelial growth factor; EGFR: EGF receptor; and VEGFR: VEGF receptor).